
This is an electronic reprint of the original article.
This reprint may differ from the original in pagination and typographic detail.

Astikainen, Oskar; Klemettinen, Lassi; Tammela, Joonas; Taskinen, Pekka; Michallik, Radoslaw M.; O'Brien, Hugh; Lindberg, Daniel

Industrial Department of Minor and Trace Elements in Direct Nickel Matte Smelting

Published in:
JOM

DOI:
[10.1007/s11837-024-06739-4](https://doi.org/10.1007/s11837-024-06739-4)

Published: 01/09/2024

Document Version
Publisher's PDF, also known as Version of record

Published under the following license:
CC BY

Please cite the original version:
Astikainen, O., Klemettinen, L., Tammela, J., Taskinen, P., Michallik, R. M., O'Brien, H., & Lindberg, D. (2024). Industrial Department of Minor and Trace Elements in Direct Nickel Matte Smelting. *JOM*, 76(9), 5445–5458. <https://doi.org/10.1007/s11837-024-06739-4>

This material is protected by copyright and other intellectual property rights, and duplication or sale of all or part of any of the repository collections is not permitted, except that material may be duplicated by you for your research use or educational purposes in electronic or print form. You must obtain permission for any other use. Electronic or print copies may not be offered, whether for sale or otherwise to anyone who is not an authorised user.



TECHNICAL ARTICLE

Industrial Department of Minor and Trace Elements in Direct Nickel Matte Smelting

OSKAR ASTIKAINEN,^{1,2} LASSI KLEMETTINEN ,^{1,4}
JOONAS TAMMELA,² PEKKA TASKINEN ,¹
RADOSLAW M. MICHALLIK,³ HUGH O'BRIEN ,³
and DANIEL LINDBERG ¹

1.—Department of Chemical and Metallurgical Engineering, Aalto University, P.O. Box 16100, 00076 Aalto, Finland. 2.—Boliden Harjavalta, 29800 Harjavalta, Finland. 3.—Finnish Geological Survey, Vuorimiehentie 2 K, 02150 Espoo, Finland. 4.—e-mail: lassi.klemettinen@aalto.fi

A sampling campaign was carried out at an industrial nickel flash smelter with the aim of evaluating the trace element distributions along the smelting line from raw materials to high-grade nickel matte and discard slag. The industrial technology was direct-to-nickel matte smelting without conventional Peirce–Smith converters, thus having two different nickel mattes as smelting products and feeds in the refinery: the sulfidic low-iron nickel matte from smelting furnace and the low-sulfur electric furnace matte from slag cleaning. Major and trace element concentrations were obtained from the solidified samples by electron probe microanalysis and laser ablation–inductively coupled plasma–mass spectrometry. Due to the industrial sampling environment, i.e., the slow cooling rate of the samples, not all the trace element concentrations were able to be measured at the lowest detection limits of the techniques used in some of the phases formed after cooling. However, the obtained results and element distribution coefficients were in good agreement with equilibrium values published in the literature.

INTRODUCTION

In flash smelting, finely ground charge material is fed through the concentrate burner into the furnace, where it is dispersed, heated, and ignited. Most of the energy needed to smelt the mineral charge is produced by the exothermic oxidation of sulfur and iron. Two flash smelters have adopted the direct Outotec nickel (DON) smelting technology, where the flash smelting furnace (FSF) produces in one step a low-iron matte for hydrometallurgical refining.¹ The DON process was originally developed for low-copper, high-MgO concentrates due to its ability to better oxidize iron to the slag, diluting the MgO concentration of slag and lowering its liquidus

temperature. Today, the DON technology can be used for a wide range of nickel sulfide concentrates.^{1,2}

Due to the oxidizing environment in the FSF, the nickel concentration in the DON slag is high. Thus, the FSF slag is cleaned in an electric slag cleaning furnace (EF) using coke as a reductant to recover the valuable metals.^{1,3} The DON process has several benefits when it comes to the recovery of valuable metals. Losses of precious metals (Au, Ag, Pt, and Pd) to slags have been shown to be lower when producing low-iron mattes compared to high-iron mattes,⁴ and, e.g., cobalt recovery is higher due to small internal circulations.¹

Many sulfidic nickel concentrates contain significant amounts of MgO, and the silica sand used as a flux contains, e.g., K₂O as an impurity. The DON smelting slags typically contain between 5 and 10 wt.% MgO, depending on the raw material basis. A higher MgO concentration has been shown to raise the liquidus temperature and apparent

viscosity, leading to higher operating temperature.¹ This is explained by formation of a stable magnesium olivine (forsterite) phase with a high melting point.

The aim of this study was to examine the development of phase assays in the nickel matte smelting from DON FSF products to slag cleaning EF. The information is crucial when optimizing the operational conditions of the smelter for maximizing the recoveries of the main and minority metals. Such industrial data are rare in nickel matte smelting operations for which only two previous papers were located.^{2,5} The focus of this work was the distributions of trace elements in the matte–slag systems of the DON process.

The Trace Element Distributions in Nickel Matte Smelting

Limited data exist in the literature regarding the distribution behavior of industrially relevant trace elements in nickel matte smelting. However, the smelting conditions of copper matte making and (high-grade) nickel matte smelting in DON technology are close to each other if the iron in the matte is used as a variable for the degree of oxidation instead of 'matte grade', as discussed in a recent conference paper.⁶ This can also be concluded from the similar magnetite contents of the slags. Therefore, selected papers on trace element distributions in copper smelting were also considered for reference in this work.

Font et al.⁷ measured the slag-to-matte distribution coefficient, $L_{As}^{s/m}$, for arsenic between iron-silicate slag and nickel matte at 1300°C, at a range of pSO_2 . At all pSO_2 , the distribution moved toward the matte at higher matte grades. Hidayat et al.⁸ equilibrated industrial nickel converter mattes with industrial converter slags and studied the effect of CaO fluxing on the distribution behavior of As. The addition of up to 30 wt.% CaO did not significantly change the behavior of the arsenic, which mostly departed to the matte phase.

Sukhomlinov et al.⁹ studied the behavior of lead in a nickel–copper matte–slag system, obtaining distribution coefficient values, $L^{m/s}$, close to unity despite significant volatilization of Pb. Kaur et al.¹⁰ reviewed the literature on the distribution of lead between copper and iron silicate and calcium ferrite slags at 1300°C and $pO_2 = 10^{-6}$ atm. Monzen et al. investigated the distribution of lead between copper mattes and slags,¹¹ and discovered that sodium addition to the slag decreases volatilization and slagging of Pb. Kudo et al.¹² studied the solubility of lead in iron-saturated silicate slags, and their results also suggested that slagging of lead is more effective with acidic slags compared to basic ones.

Sukhomlinov et al.⁹ studied selenium distribution at 1400°C between nickel–copper matte and iron silicate slags containing MgO and K_2O , at a fixed pSO_2 and pO_2 . The copper–nickel ratio in the matte

was 0.19 (w/w), and the selenium was found to strongly associate with the matte. The distribution coefficient, $L^{m/s}$, showed a slight increase when adding MgO or K_2O in the slag. The distribution coefficient, $L_{Se}^{m/s}$, determined by Choi and Cho¹³ was much lower than that determined by Sukhomlinov et al.,⁹ although selenium still showed a clear preference to matte over slag, especially at high matte grades and temperatures. The discrepancy can be explained by differences in the experimental procedures.

Font and Reddy determined the matte–slag distribution coefficient for antimony between nickel–matte and a MgO-containing iron silicate slag.¹⁴ The measurements were performed at 1300°C, over a range of pO_2 from 4.5×10^{-9} to 2.4×10^{-8} atm. This range of pO_2 was similar to that used in the reductive step of the EF operation ($10^{-8.5}$ – 10^{-8} atm), while the FSF is operated at significantly more oxidizing conditions with pO_2 between 10^{-7} and 10^{-6} atm.² The $L_{Sb}^{m/s}$ showed a strong increasing trend with increasing pO_2 .¹⁴ Font et al.⁷ determined $L_{Sb}^{s/m}$ between iron silicate slag and nickel matte in a range of pSO_2 at 1300°C. Kaur et al. reviewed the literature on the distribution of antimony between copper and iron silicate and calcium ferrite slags at 1300°C and $pO_2 = 10^{-6}$ atm.¹⁰ They suggested that increased slag basicity increases the deportment of Sb in the slag.

Choi and Cho¹³ studied the distribution of cobalt between a nickel–copper–iron matte and silica-saturated iron silicate slags at 1250°C. They also studied the effect of different fluxes on $L_{Co}^{m/s}$. Font et al.⁷ determined the slag–matte distribution coefficients for cobalt between iron silicate slag and nickel matte at 1300°C and a range of pSO_2 . The predominant form of cobalt was CoO in the slag and $CoS_{2/3}$ in the matte. Taskinen et al.⁶ presented matte–slag distribution coefficients for cobalt between nickel matte and iron silicate slag with MgO concentrations of 0, 4, and 8.5 wt.%, based on the results of Piskunen et al.⁴ The experiments were conducted at 1400°C, at silica saturation and with Ni/Cu = 4 (w/w). Sukhomlinov et al. studied the distribution of cobalt at 1400°C between nickel–copper matte and iron silicate slags ($L^{m/s}$) with MgO and K_2O , at fixed pSO_2 and pO_2 .⁹ The ratio between copper and nickel in the matte was 0.19 (w/w).

The matte-to-slag distribution data of copper are available for FSF conditions in most of the papers cited above. For EF conditions with low sulfur concentrations, alloy-to-slag data have also been measured by a few authors.^{15–17}

The nature of EF mattes, due to their low sulfur concentration, is close to metal alloys. Thus, their thermodynamic properties and, e.g., distribution coefficients with slags are different from the FSF matte and also depend on the extent of reduction in the EF batch process, i.e., the end point of magnetite in the discard slag and the iron concentration of the matte.^{15,17,18} Thus, any extrapolation of, e.g., the

distribution coefficient values from FSF to EF is impossible, and for that purpose the measured values of alloy–slag equilibria are needed^{15,16,19} as a function of iron concentration of the EF matte for comparing the obtained results.

EXPERIMENTAL

The sampling campaign was carried out at the Boliden Harjavalta Smelter Nickel line in summer 2023. Scanning electron microscopy–energy dispersive spectroscopy (SEM-EDS), electron-probe microanalysis (EPMA), and laser ablation–inductively coupled plasma–mass spectrometry (LA-ICP-MS) were used to quantify the concentrations of trace elements in the matte and slag. SEM-EDS was used to characterize the phases, and the ratios of the phases were determined from the back-scattered electron (BSE) images taken with SEM. EPMA and LA-ICP-MS were used to determine the phase-specific concentrations. The knowledge of the ratios between the different phases and of their chemical compositions were used to determine the bulk concentrations of each trace element of interest.

The samples were taken in matte–slag pairs to make sure that the samples represent the same feed. They contained two matte–slag pairs for both the FSF and EF. This study used two distinct sampling techniques. The first technique, which was used for all FSF and EF slag samples and the FSF mattes, was to take samples from the melt during tapping. A relatively small steel sampling ladle was used, and the samples were taken around the halfway point of the tapping, to make the sample as representative as possible of the overall composition of the matte and slag. The samples were left to cool in air, before being crushed to an appropriate particle size. The alternative sampling technique was to recover the matte after granulation. The furnace temperatures during sampling were $1430 \pm 15^\circ\text{C}$ and $1410 \pm 4^\circ\text{C}$ for FSF and EF, respectively. The oxygen enrichment of FSF reaction shaft was $90 \pm 1 \text{ vol}\%$.

The bulk concentrations of the main components were determined by X-ray fluorescence spectrometry (XRF; Zetium XRF Elemental Analyzer; Malvern PANalytical, UK). The magnetite concentrations shown in Table I were measured with a Satmagan 135 (Rapiscan Systems, USA).

The sample preparation for SEM-EDS, EPMA, and LA-ICP-MS was carried out using standard wet methods using SiC papers for grinding down to 4000 grit with water as lubricant, followed by 3- and 1- μm diamond sprays on cloth for polishing. The carbon coating was performed with an IB-29510VET vacuum evaporator (JEOL, Japan). The coating was finished once the brass cylinder used as an indicator had reached a purple color, indicating an optimal film thickness.

The microstructures were analyzed with SEM (Mira3; Tescan, Czech Republic) with a Schottky emission source, and the preliminary elemental concentrations were determined with an UltraDry Silicon Drift EDS (Thermo Fisher Scientific, USA). The analyses were performed using an acceleration voltage of 15 kV and a beam current of 9.4 nA. The standards used in the EDS measurements are set out in Supplementary Table S-I (refer to online supplementary material). The EPMA analysis was performed using a JXA-iHP200F Schottky-type FEG-EPMA (JEOL, Japan) equipped with five WDS detectors. An acceleration voltage of 15 kV and a beam current of 15 nA were used. The point measurements were taken with defocused beam diameters of 1, 3, 5, 10, and 20 μm , depending on the sizes of the phase areas. The primary data were corrected with the XPP on-line matrix correction program.²⁰ Natural and synthetic minerals and metals were used as external standards (see Supplementary Table S-II). The background correction was carried out by the mean atomic number (MAN) correction method.²¹ A total of 211 measurement points were taken with EPMA, with an average of 6 points per phase.

The quantified element maps were generated using the Probe for EPMA software (www.probesoftware.com) by John Donovan. The measurements were done using a focused beam with a beam current of 100 nA and an accelerating voltage of 15 kV. The background correction was done using the MAN correction method.²¹ The maps had a size of 213×160 pixels. The pixel parameters used for each sample are collected in Supplementary Table S-III.

The trace element analysis was performed using a LA-ICP-MS system consisting of an AttoM single-collector ICP-MS (Nu Instruments, UK) coupled with a Photon Machines 193-nm ArF excimer laser ablation system (Teledyne CETAC Technologies, USA). The analysis protocol was roughly the same for all the samples: the sequence started with five pre-ablation pulses to remove the carbon coating, followed by 20 s of flushing the ablation chamber, 20 s of background analysis, and 12 or 30 s of trace element analysis (120 or 300 laser shots at 10 Hz). Some phase areas were very small, posing challenges for the laser ablation. Generally, a 20- μm laser spot size was used, but, for one sulfide phase, a 10- μm spot (with 120 laser shots) had to be utilized. The analysis of one phase was succeeded by 2–3 spots taken from an external standard and a total of 4–5 spots taken from 2 to 3 verified reference materials analyzed as unknowns and used to verify the results. The internal and external standards as well as the reference materials used are shown in Supplementary Table S-IV, and the operation parameters have been set out in Supplementary Table S-V.

Table I. XRF analyses for the mattes and slags

Sample name	Mattes, wt.%				
	Ni	S	Cu	Fe	Co
FSF Matte 1	54.9	23.8	11.9	7.4	
FSF Matte 2	57.9	23.1	12.1	5	
EF Matte 1	42.6	5.5	6.1	39.2	4
EF Matte 2	45.7	5.4	6.7	36.7	3.9

Sample name	Slags, wt.%							
	Fe	SiO ₂	MgO	Ni	CaO	Al ₂ O ₃	Fe ₃ O ₄	Fe/MgO
FSF Slag 1	37.3	31.1	8.1	3.2	2.4	2.1	11	4.6
FSF Slag 2	36.9	30.8	8	4	2.3	2.1	11	4.6
EF Slag 1	38.9	33	8.6		2.5		2	4.5
EF Slag 2	37.4	34.2	8.9		2.8		3	4.2

The isotopes to be analyzed were chosen so that the interferences between mono- and polyatomic ions of similar mass-to-charge ratios could be minimized, using an in-built interference calculator of the ICP-MS software. A relatively comprehensive list of the known polyatomic interferences has also been prepared by May and Wiedmeyer.²² The following isotopes were used to define the composition of the samples, with the bolded ones being the main trace elements of interest: ²³Na, ²⁶Mg, ²⁷Al, ²⁹Si, ³⁴S, ³⁹K, ⁴⁴Ca, ⁴⁹Ti, ⁵⁹Co, ⁶²Ni, ⁶⁵Cu, ⁶⁷Zn, ⁷⁵As, ⁷⁷Se, ¹²¹Sb, and ²⁰⁸Pb.

The raw data from the mass spectrometer in the form of time-resolved analysis signal (counts per second) was processed using the GLITTER data reduction software.²³ The signal was processed manually for each point by choosing the part of the signal to be included in the elemental concentration results, and what part was considered as background signal.

RESULTS AND DISCUSSION

The XRF data, gathered as a part of the normal operation of the smelter, is presented in Table I to give a rough estimate of the concentrations of the main components. The data is based on industrial samples, which were taken at roughly the same time as the analyzed samples.

Phase Characterizations and Distribution of Trace Elements

Utilization of Quantified Elemental Maps

An example of the utilization of quantified elemental maps is shown in Supplementary Fig. S-1. In this example, the maps are used for the calculation of average phase composition of heterogeneous

fayalite crystals. Four different, manually drawn, areas are shown along with the number of pixels within each area. The Probe for EPMA software calculated the average composition within one selected area at a time, and the final composition was calculated by taking a weighted average (according to number of pixels) of the four areas. This method was used for major element concentration quantifications in heterogeneous phases. As the dwell time per pixel was only 100 ms, the elemental detection limits were approximately one order of magnitude higher than in the EPMA point measurements. Therefore, trace element concentrations in these phases were taken from point measurements or from the LA-ICP-MS data.

Flash Smelting Furnace

The phases present in each sample were identified based on the BSE images produced by SEM. The samples had complex structures, with more than four phases identified by mineralogical observations. The average major element stoichiometries of the phases were calculated from the EPMA element maps for the heterogeneous phases and from the EPMA point measurements for the homogeneous phases. Due to high elemental detection limits, trace elements could not be reliably quantified from the element maps. The phase fractions were calculated statistically: a grid was overlaid on the BSE images, and the number of grid points falling in each of the phases were calculated. The ratios between the number of grid points were calculated and taken to represent the area ratios of the phases. A 23 × 23 grid was used, and 8 images were analyzed per sample, giving a total of 4232 data points for each of the samples.

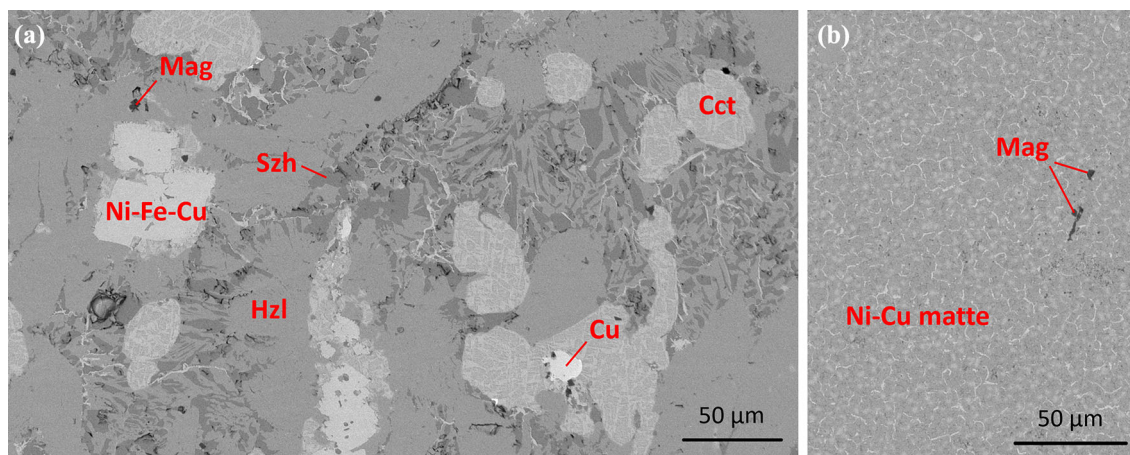


Fig. 1. (a) SEM-BSE image of the first FSF matte sample showing each of the six identified phases: chalcocite (Cct), Ni-Fe-Cu alloy, shenzhuangite (Szh), heazlewoodite (Hzl), magnetite (Mag), and copper alloy (Cu). (b) SEM-BSE image of the granulated FSF matte of the second sampling, showing the two identified phases.

Table II. Compositions and fractions of phases in the first (slowly cooled) and second (granulated) FSF matte

Phase	1st FSF matte, slowly cooled						2nd FSF matte, granulated	
	Cct	Ni-Fe-Cu	Szh	Hzl	Mag	Cu	Ni-Cu matte	Mag
Area%	15.3	7.9	16.1	60.5	0.08	0.12	~ 99	~ 1
As	31	56	< 0.38 wt.%	191	< 0.37 wt.%	< 0.40 wt.%	164	< 0.37 wt.%
Co	480	8456	1.94 wt.%	5368	0.20 wt.%	616	4646	0.4 wt.%
Cu	69.4 wt.%	7.9 wt.%	1.8 wt.%	0.9 wt.%	< 574	97.0 wt.%	11.2 wt.%	0.5 wt.%
Fe	6.9 wt.%	15.7 wt.%	31.2 wt.%	0.8 wt.%	69.9 wt.%	1.1 wt.%	3.9 wt.%	66.4 wt.%
Ni	0.7 wt.%	74.8 wt.%	31.8 wt.%	70.4 wt.%	3.1 wt.%	0.9 wt.%	59.5 wt.%	5.6 wt.%
Pb	25	2.1	< 2040	143	< 230	< 255	151	< 230
S	22.2 wt.%	< 387	32.5 wt.%	26.9 wt.%	0.2 wt.%	0.1 wt.%	24.3 wt.%	0.5 wt.%
Sb	4.1	6.8	< 173	19	< 157	226	19	< 158
Se	746	< 30	0.1 wt.%	621	< 228	< 278	589	< 229
Zn	291	< 25	< 444	46	< 430	913	50	< 431
O	0.4 wt.%	< 470	0.4 wt.%	0.1 wt.%	26.6 wt.%	0.3 wt.%	0.2 wt.%	26.5 wt.%

The values in bold are LA-ICP-MS data (ppmw) and the rest are based on EPMA (ppmw if no unit has been given, otherwise wt.%). The smaller than symbol (<) refers to the detection limit.

As seen in Fig. 1a, six phases were identified in the first FSF matte sample by EPMA and SEM-EDS. The major phases were heazlewoodite (Hzl; Ni_3S_2), shenzhuangite (Szh; NiFeS_2), chalcocite (Cct; $\text{Cu}_2\text{S-FeS}$), and a metal alloy of nickel, iron, and copper. Additionally, two minor phases, copper (Cu) and magnetite (Mag; Fe_3O_4) were identified. Chalcocite, the Ni-Fe-Cu alloy, and heazlewoodite form large grains in the slowly cooled samples, while shenzhuangite was dispersed as smaller grains within the heazlewoodite. Table II shows the elemental compositions of the phases in the first FSF matte as well as the second (granulated) FSF matte, based on the LA-ICP-MS and EPMA results. An SEM image of the second slowly cooled FSF matte sample is shown in Supplementary Fig. S-2, and its phase area fractions as well as phase

compositions are shown in Supplementary Table S-VI.

The same phases as in the first slowly cooled FSF matte sample were identified in the second one. However, their fractions varied significantly, the main differences being a much lower fraction of shenzhuangite (3.9 area%) and the higher fraction of heazlewoodite (70.6 area%). The granulated version of the second FSF matte had a relatively homogeneous structure due to the rapid cooling. Thus, only one major phase was found (see Fig. 1b). This Ni-Cu matte had a relatively similar stoichiometry as heazlewoodite in the slowly cooled sample. Due to rapid quenching, the Ni-Cu matte contained significant amounts of Cu_2S and FeS , which separated into their own phases during cooling. The granulated sample also contained

magnetite as a minor phase. The area ratio of the magnetite phase could not be determined exactly and was approximated to 1 area%.

The main phases in the solidified FSF slag samples were fayalite (Fa), intergranular glass (Gls), and magnetite (Mag). Additionally, the FSF slags contained entrained matte as a minor phase. It should be noted that, from a mineralogical perspective, the use of the name fayalite is not entirely correct, as this phase also contains a significant amount of forsterite (Mg_2SiO_4), and therefore a more correct name would be olivine [solid solution where the end members of this study are, e.g., fayalite (Fe_2SiO_4), forsterite, and nickel olivine (Ni_2SiO_4)]. However, as these types of slags are commonly referred to as 'fayalite slags' in metallurgical literature, the name fayalite (Fa) will be used throughout the manuscript. The four phases identified in the first FSF slag sample are marked on the BSE images shown in Fig. 2, and the elemental concentrations in each phase of the first and second FSF slag are presented in Table III. As seen in Fig. 2, the fayalite crystals are much larger in the first FSF slag, possibly indicating a slower cooling rate.

The fayalite crystals displayed a clear concentration gradient when moving towards the edges of the phase. The gradient is further visualized in Fig. 3, where the lighter gray edges of the fayalite grains indicate a higher average atomic number compared to the darker center part. The quantitative element maps in Fig. 3 indicate that the lighter areas contain higher concentrations of iron and lower concentrations of magnesium and nickel.

The concentration of selenium was too low in the FSF slags to be accurately determined with the small laser spot used. Within the slag, cobalt distributed mainly in fayalite and the minor phase magnetite. Lead, arsenic, and antimony distributed towards the intergranular glass, while zinc

distributed evenly between the fayalite and the intergranular glass.

Electric Furnace

The quenched EF matte samples had simpler microstructures than the slowly cooled FSF samples, due to the rapid cooling. A BSE image of the first EF matte sample is shown in Fig. 4a, with labels of the identified phases. The Ni-Fe-Co-Cu alloy phase occupies roughly 80% of the total cross-sectional areas of both the EF matte samples post-cooling and the rest is filled by the Fe-Ni-Cu sulfide. For this sulfide, a very small 10- μm laser spot size had to be chosen due to the small size of the phase areas. Selenium, zinc, lead, and antimony distributed preferentially in the sulfide in the solidified EF matte, while cobalt departed in the alloy and arsenic was distributing evenly between both the phases.

The BSE image for the second EF matte is shown in Fig. 4b, and the stoichiometries as well as the area ratios of the phases are shown in Table IV. A segregated phase enriched in copper was identified in the microstructure of the sulfide, locating on grain boundaries. It consisted of Cu_2S , FeS, and Ni_3S_2 in the mass ratio of 8.7:6:1. The precipitate was uniformly distributed within the continuous sulfide phase. Its morphology and chemical composition can be best visualized from the quantified elemental maps shown in Fig. 5. A similar grain boundary phase was present in the first matte sample, although its phase fraction was much less than in the second sample. In Table IV, the results for the sulfide phase also include this segregated phase.

The phases in the EF slags exhibit somewhat similar stoichiometries as the FSF slags, but their phase fractions differ significantly. The fayalite phase in the EF slag is purer and contains lower concentrations of nickel and magnesium and a

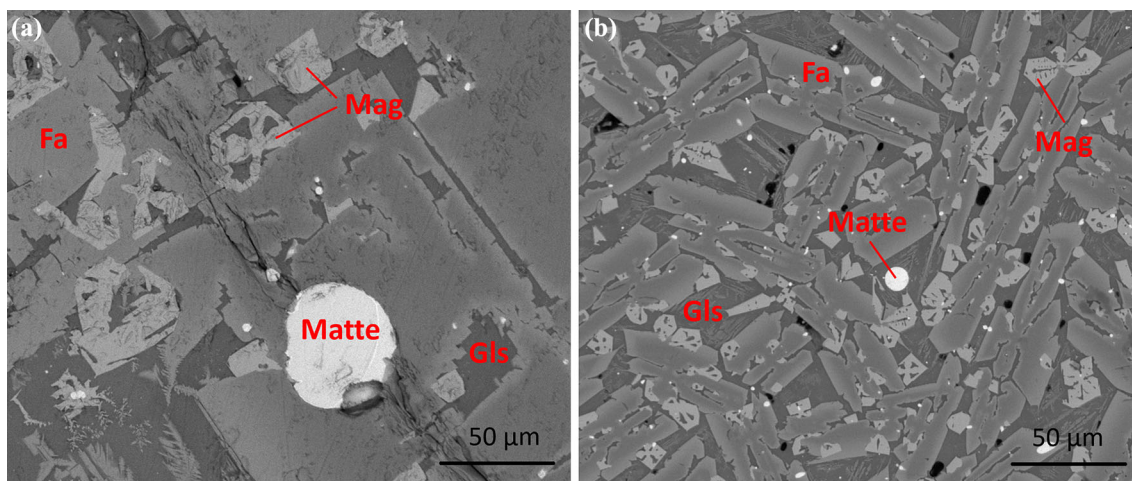


Fig. 2. SEM-BSE images of the first (a) and second (b) FSF slag samples showing the identified phases: fayalite (Fa), intergranular glass (Gls), magnetite (Mag), and mechanically entrained matte.

Table III. Compositions and fractions of the phases in the FSF slags

Phase	1st FSF slag				2nd FSF slag			
	Fa	Gls	Mag	Matte	Fa	Gls	Mag	Matte
Area%	68.1	21.0	10.0	0.9	64.9	23.3	11.4	0.4
Al	0.11 wt.%	3.9 wt.%	1.4 wt.%	< 124	0.51 wt.%	3.1 wt.%	1.4 wt.%	< 142
As	4.0	12.1	< 0.40 wt.%	< 0.40 wt.%	6.0	26	< 0.40 wt.%	< 0.40 wt.%
Ca	0.2 wt.%	9.5 wt.%	467	< 170	0.2 wt.%	9.6 wt.%	834	528
Co	7045	590	3555	0.3 wt.%	5889	822	3495	273
Cu	363	1617	< 348	36.7 wt.%	1170	0.6 wt.%	< 379	76.8 wt.%
Fe	40.1 wt.%	19.9 wt.%	66.3 wt.%	4.6 wt.%	31.9 wt.%	22.5 wt.%	66.4 wt.%	3.3 wt.%
K	372	1.4 wt.%	< 71	< 79	0.19 wt.%	1.0 wt.%	< 142	< 90
Mg	6.7 wt.%	0.1 wt.%	0.4 wt.%	< 153	9.9 wt.%	0.2 wt.%	0.43 wt.%	< 174
Na	284	0.9 wt.%	< 212	< 258	0.13 wt.%	0.7 wt.%	< 213	433
Ni	3.8 wt.%	153	1.9 wt.%	34.7 wt.%	7.5 wt.%	919	2.4 wt.%	0.17 wt.%
Pb	3.8	256	< 229	0.1 wt.%	122	992	< 229	0.1 wt.%
S	< 72	0.1 wt.%	< 84	23.2 wt.%	< 83	0.1 wt.%	< 205	19.2 wt.%
Sb	< 0.3	8.9	< 156	< 211	5.4	39	< 157	< 232
Se	< 0.58	< 1.5	< 224	0.1 wt.%	1.1	< 1.2	< 225	755
Si	14.7 wt.%	23.0 wt.%	0.3 wt.%	< 119	15.4 wt.%	22.3 wt.%	0.4 wt.%	255
Zn	980	969	< 436	< 451	1677	1739	< 530	< 578
O	33.8 wt.%	40.5 wt.%	28.0 wt.%	0.17 wt.%	34.3 wt.%	39.2 wt.%	27.4 wt.%	< 519

The bold values are LA-ICP-MS data (ppmw) and the rest are EPMA data (ppmw if no unit has been given, otherwise wt.%).

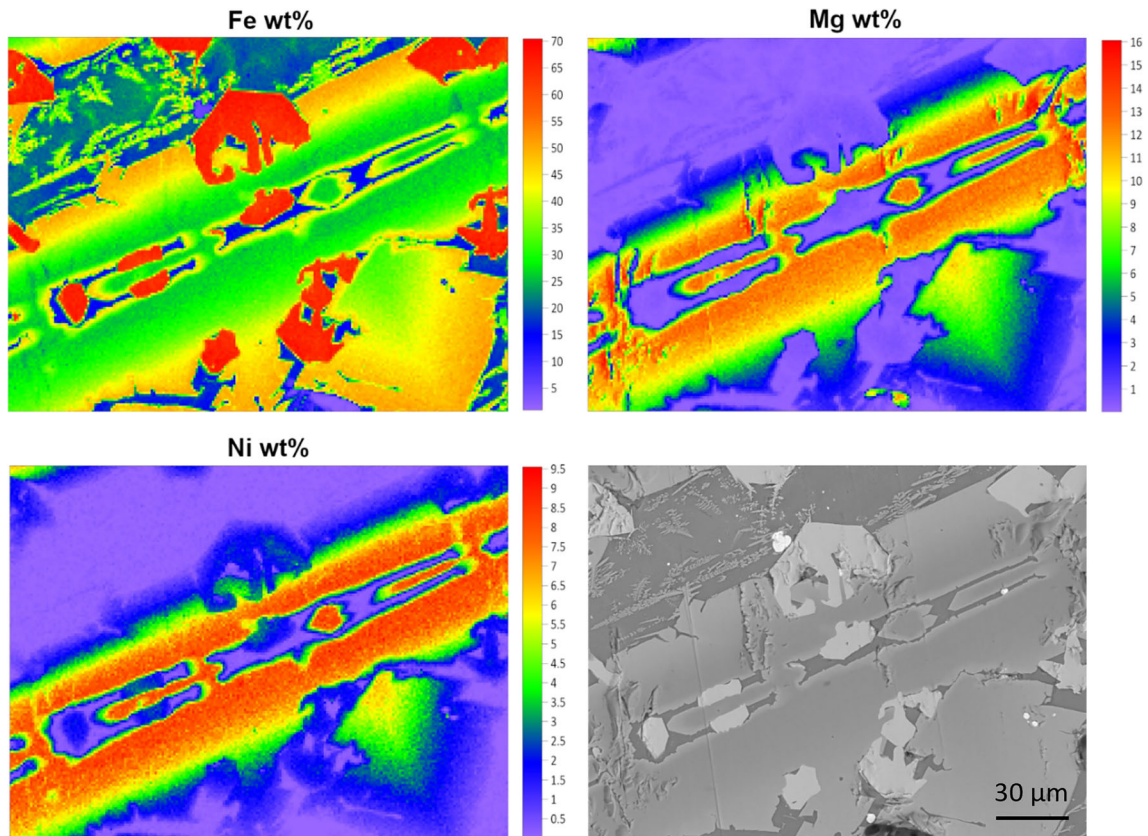


Fig. 3. Quantified EPMA elemental maps for the first FSF slag, showing the concentration gradients for iron, magnesium, and nickel within the fayalite grains; alongside is the corresponding BSE image.

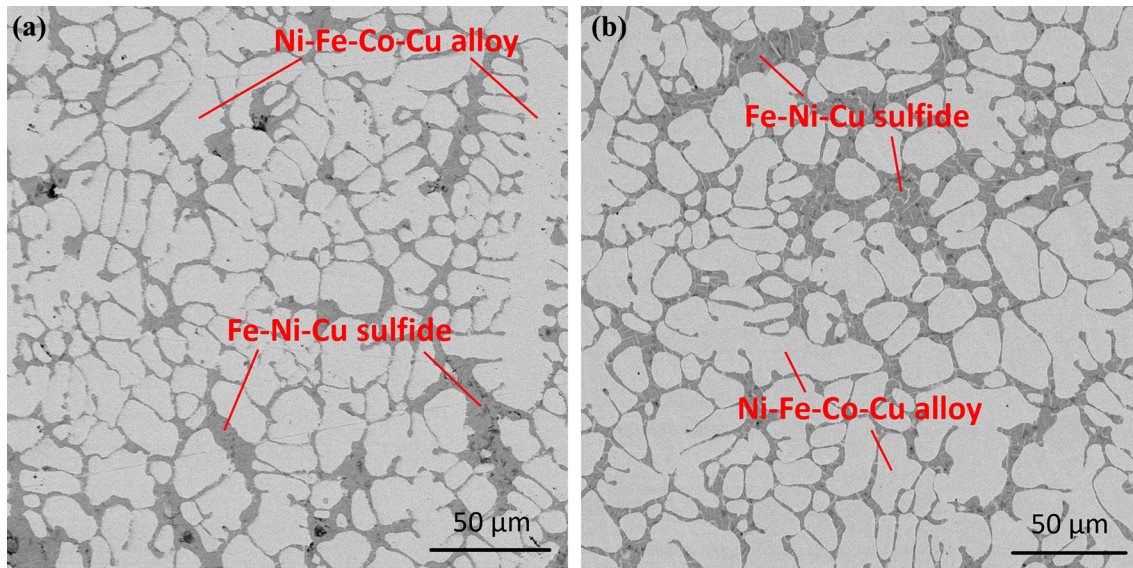


Fig. 4. SEM-BSE images of the microstructures of the first (a) and second (b) quenched (granulated) EF mattes. Segregation within the sulfide phase is visible in the second EF matte.

Table IV. Compositions and area fractions of the phases in the EF mattes

Phase	1st EF matte		2nd EF matte	
	Alloy	Sulfide	Alloy	Sulfide
Area%	79.8	20.2	79.3	20.7
As	125	88	48	93
Co	5.6 wt.%	1.7 wt.%	5.4 wt.%	2.0 wt.%
Cu	4.8 wt.%	13.2 wt.%	5.1 wt.%	12.1 wt.%
Fe	44.2 wt.%	35.0 wt.%	41.5 wt.%	30.7 wt.%
Ni	45.6 wt.%	19.2 wt.%	48.2 wt.%	24.5 wt.%
Pb	25	3206	19	2555
S	0.1 wt.%	29.0 wt.%	663	30.3 wt.%
Se	76	604	52	615
Sb	83	455	26	498
Zn	238	572	274	927
O	< 446	2.1 wt.%	448	0.6 wt.%

The bold values are the LA-ICP-MS results (ppmw) and the rest are based on EPMA (ppmw if no units are given, otherwise wt.%).

higher concentration of iron, due to the slag cleaning conditions and recovery of nickel. The intergranular glass in the EF slags had a slightly higher concentration of alumina but otherwise it was similar to that of the FSF slags. The amount of magnetite in the EF slags was obviously much lower compared to the FSF slags, and the composition of magnetite in the EF slag also differed from the FSF slag. In both EF slag samples, the magnetite contained more aluminum and titanium, and was depleted of nickel and cobalt. In the first EF slag sample, the magnetite contained more than twice as much titania and almost twice as much alumina as in the second sample, showing a higher degree of reduction.

In both EF slag samples, the intergranular glass contained large amounts of dispersed fayalite. This was especially true for the second EF slag where large areas of pure glass were difficult to find. The BSE images of the first and second EF slags are shown in Fig. 6, with labels of each identified phase. The area fractions and elemental compositions of the phases are shown in Table V.

The phase fractions of fayalite and intergranular glass in both EF slag samples were the almost the same (80.1 and 80.7 area% for fayalite and 17.5 and 17.1 area% for glass, respectively). Differences were found in the phase fractions of magnetite (1.0 and 1.7 area%) as well as entrained matte (1.4 and 0.5 area%, respectively) in the investigated cross-sections.

Considering the two main phases, fayalite and glass, which had a large enough size to be analyzed with LA-ICP-MS, selenium and lead distributed mainly in the intergranular glass, and arsenic to the fayalite. Zinc distributed evenly between the two main phases, and cobalt mainly to the fayalite and the minor phase to the magnetite. It can be seen in Table V that the cobalt concentration in the entrained matte was more than one order of magnitude higher than in the slag.

As seen in the quantified element maps of Fig. 7, the concentration gradients of iron and magnesium in the precipitates are less distinct in EF slags compared to the FSF slags. The presence of fayalite and magnetite crystals within the intergranular glass can be evaluated clearly in the quantified elemental map of iron. The composition of the dispersed fayalite appears to differ only slightly from the large fayalite grains, especially by their lower magnesium concentrations. Nickel favors fayalite and occurs at slightly higher concentrations

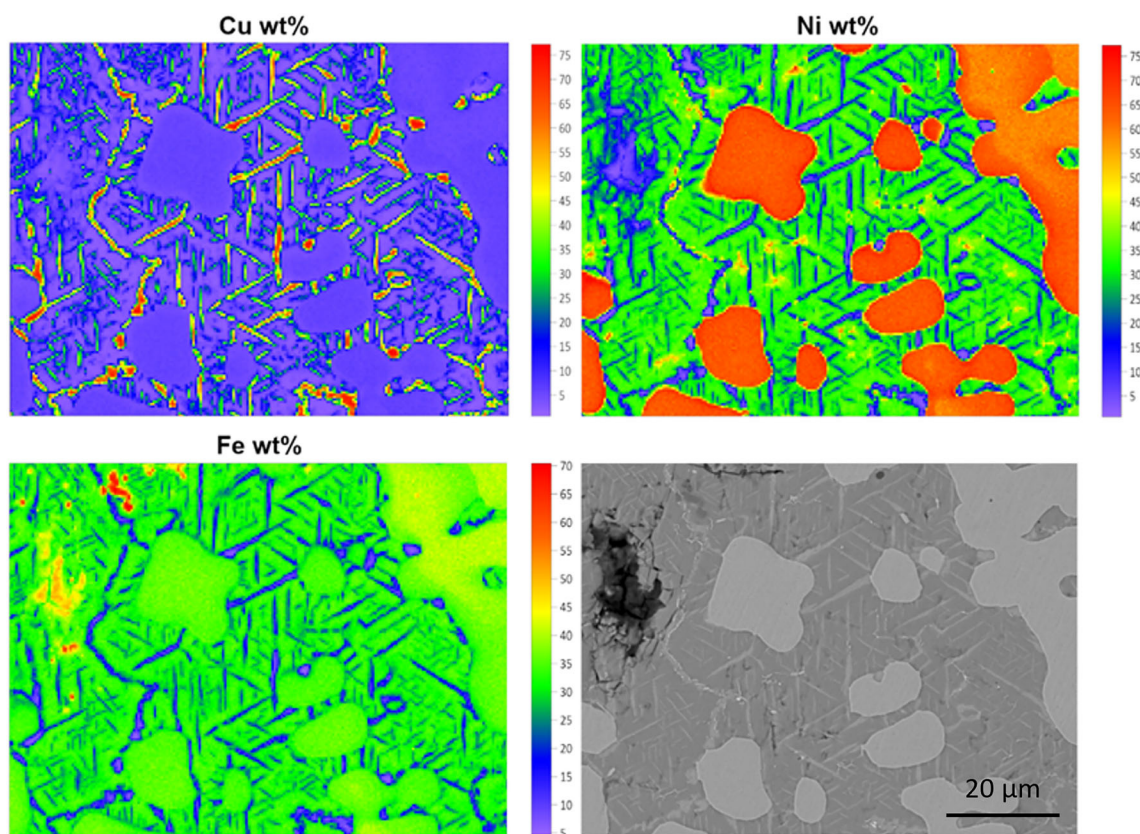


Fig. 5. Quantified elemental maps (EPMA) of the second EF matte, showing the distinct copper-rich segregation within the sulfide matrix, on its grain boundaries during quenching; the large nickel-rich precipitates represent the FeNi alloy (close to FeNi_3 , awaruite) formed during quenching.

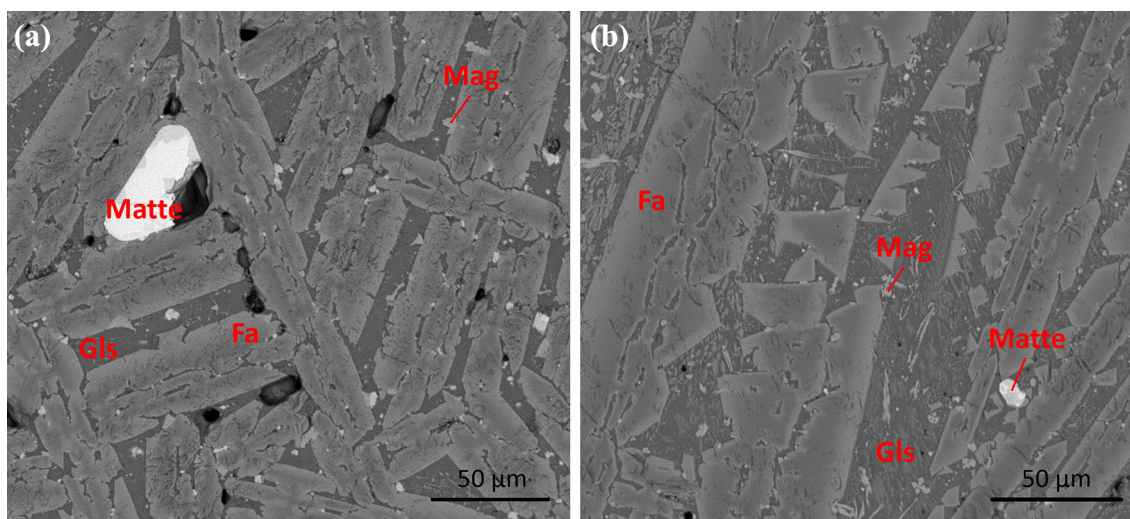


Fig. 6. SEM-BSE images of first (a) and second (b) EF slag samples; the fayalite (Fa), intergranular glass (Gls), magnetite (Mag), and entrained matte are identified.

in the magnesium-rich areas of the fayalite grains. It must be pointed out that the fayalite grains did form during the cooling and solidification of the slag and that time-dependent process explains the concentration patterns and their complexity.

Distributions Between Mattes and Slags

The calculated distribution coefficients of this study for each trace element studied are set out in Table VI. The data were extracted from the matte–slag pairs of the FSF and EF samples. The

Table V. Compositions and area fractions of the phases in the EF slag samples

Phase	1st EF slag				2nd EF slag			
	Fa	Gls	Mag	Matte	Fa	Gls	Mag	Matte
Area%	80.1	17.5	1.0	1.4	80.7	17.1	1.7	0.5
Al	234	5.6 wt.%	3.1 wt.%	< 128	334	4.1 wt.%	1.8 wt.%	< 116
As	3.9	1.1	< 0.4 wt.%	< 0.4 wt.%	2.7	1.8	< 0.4 wt.%	< 0.4 wt.%
Ca	0.3 wt.%	9.4 wt.%	879	656	0.3 wt.%	7.6 wt.%	0.5 wt.%	272
Co	1221	153	0.1 wt.%	6.7 wt.%	2282	501	0.15 wt.%	2.7 wt.%
Cu	529	439	< 341	11.8 wt.%	127	2327	< 344	9.0 wt.%
Fe	43.6 wt.%	19.8 wt.%	58.3 wt.%	27.8 wt.%	40.0 wt.%	26.3 wt.%	63.0 wt.%	14.3 wt.%
K	0.34 wt.%	1.7 wt.%	< 103	< 146	310	1.3 wt.%	0.2 wt.%	< 78
Mg	7.1 wt.%	603	0.3 wt.%	< 155	8.9 wt.%	0.1 wt.%	0.2 wt.%	< 162
Na	0.21 wt.%	1.0 wt.%	< 203	< 336	296	0.8 wt.%	< 628	< 369
Ni	380	19	< 257	35.7 wt.%	2760	65	< 260	65.2 wt.%
Pb	21	108	< 224	0.13 wt.%	4.2	153	< 227	< 791
S	< 86	0.8 wt.%	121	16.8 wt.%	< 73	1.0 wt.%	710	8.4 wt.%
Sb	< 0.03	< 0.03	< 153	< 232	< 0.02	0.09	< 155	< 257
Se	2.1	8.4	< 215	< 319	< 1.4	6.3	< 219	< 366
Si	14.8 wt.%	20.8 wt.%	0.1 wt.%	< 878	15.0 wt.%	19.6 wt.%	1.9 wt.%	< 261
Ti	0.16 wt.%	0.8 wt.%	7.0 wt.%	< 216	208	0.6 wt.%	2.7 wt.%	< 121
Zn	392	536	< 535	< 464	539	941	< 464	< 460
O	33.9 wt.%	39.7 wt.%	30.9 wt.%	< 0.76	35.1 wt.%	38.1 wt.%	29.4 wt.%	< 0.1 wt.%

The bolded values are LA-ICP-MS data (ppmw) and the rest are based on the EPMA results (ppmw if units are not given, otherwise in wt.%).

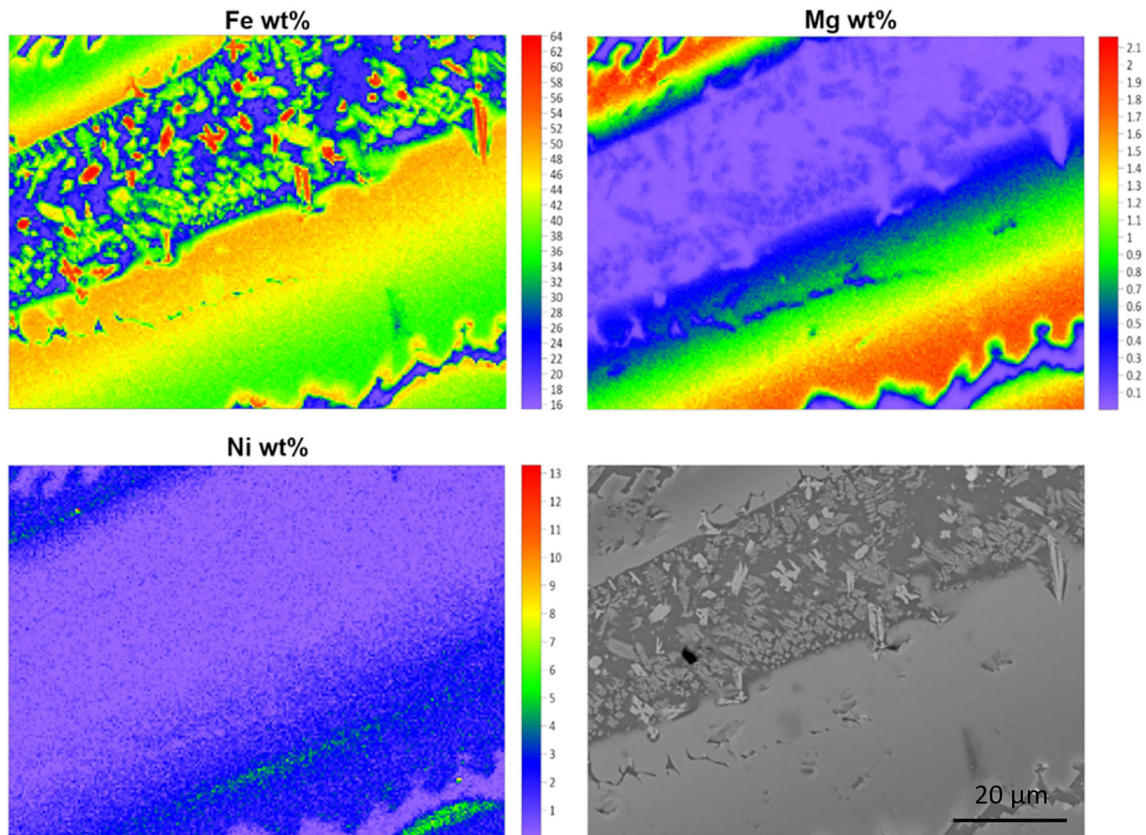


Fig. 7. Quantified element maps (EPMA) for the second EF slag sample and its fayalite grains and the intergranular glass.

Table VI. The matte-to-slag distribution coefficients obtained in this study

Matte-slag pair	FSF 1	FSF 2	FSF 2 (granulated matte)	EF 1	EF 2
$L_{As}^{m/s}$	25	12	15	34	23
$L_{Co}^{m/s}$	1.3	1.3	1.0	47	24
$L_{Cu}^{m/s}$	> 220	> 54	> 48	> 120	> 170
$L_{Pb}^{m/s}$	1.7	> 0.15	0.43	18	18
$L_{Sb}^{m/s}$	> 6.5	1.2	1.4	> 5800	> 3500
$L_{Se}^{m/s}$	> 740	> 550	> 540	57	> 76
$L_{Zn}^{m/s}$	< 0.09	< 0.04	0.03	0.73	0.67

When greater than (>) or smaller than (<) marks are used, the concentration of the element in slag or matte was below the detection limit, which means that these values are indicative only.

distribution coefficients for the second FSF and EF pairs were calculated separately, and the obtained detection limits were much lower for the quenched FSF matte. The matte–slag distribution coefficients were calculated using the results for both the slowly cooled and granulated matte and the definition is:

$$L_{Me}^{\frac{m}{s}} = [\text{wt.}\% \text{ Me}]_{\text{matte}} / (\text{wt.}\% \text{ Me})_{\text{slag}} \quad (1)$$

where $[\text{wt.}\% \text{ Me}]_{\text{matte}}$ is the concentration of Me in matte and $(\text{wt.}\% \text{ Me})_{\text{slag}}$ that in the slag.

A comparison of the distribution coefficients for the second FSF pair can be used to validate the results. These present an upper limit in the cases where the concentrations in the matte were below the detection limits; the value was replaced by the detection limit in the calculations. In such a case for the slag, the results present a lower limit. In cases where the concentrations of the element of interest were below the detection limits in both the matte and slag, the choice of which limit to represent was made based on whether the matte or the slag result are skewed more heavily due to number of points below the detection limit. Often, the observed value of distribution coefficient was close to the stated upper or lower limit, e.g., when an element distributed preferentially in one phase. The reliability of the results will be discussed on a case-by-case basis in the following paragraphs.

Since the detection limits of EPMA were several orders of magnitude higher than those of LA-ICP-MS, the EPMA data for minor phases, unable to be analyzed by LA-ICP-MS due to their size, were left out in the calculations of the distribution coefficients, except for cobalt. The concentration of cobalt was well above the detection limit of EPMA in most phases. The measured concentrations for cobalt were consistent with both analytical methods. Supplementary Table S-VII shows the phases included in the calculation of the distribution coefficients, and the total sample areas represented in the calculations.

Arsenic deported strongly in the matte and the matte–slag distribution coefficients were 18 ± 6 in

the FSF and 28 ± 6 in the EF. The FSF values are somewhat lower compared to the $L_{As}^{m/s}$ value of 38 suggested by Font et al.⁷ in their equilibrium measurements with 0.5 atm pSO₂ and 58 wt.% Ni in copper-free matte. Hidayat et al.⁸ measured even higher $L_{As}^{m/s}$ values, of > 100, when the matte contained 65 wt.% Ni. The matte–slag distribution coefficients measured in this work were lower for the second FSF matte–slag pair compared to the first one. The result was similar when using the values of the slowly cooled and the granulated FSF matte, suggesting that the deviation is not due to a measurement error. The high distribution coefficient value in the EF indicates that arsenic is effectively collected in the EF matte during slag cleaning. This is a feature often forgotten in high-temperature nickel slag cleaning processes.

The obtained distribution coefficients of copper in FSF and EF were > 48 and > 120, respectively, which are in fair agreement with the equilibrium data of Piskunen et al.⁴ at 1350–1450°C and 10 vol% SO₂, who reported values of 30 ± 10 and with Sukhomlinov et al.⁹ who reported the effects of K₂O and MgO at 1400°C on the copper distribution in FSF. In reducing conditions, in equilibrium with a low-sulfur alloy, our findings show slightly higher copper distribution coefficients than the kinetic data by Avarmaa et al.¹⁷ and the data of Pagador et al.¹⁵ at MgO saturation.

The distribution coefficients for lead determined in this work, about 1 in FSF and 18 in EF, are well in line with the equilibrium results in the literature. The matte–slag distribution coefficient determined by Chen et al.²⁴ between Pierce–Smith copper converting slags and entrained matte were between 0.15 and 2. Shuva et al.²⁵ reported a range of 0.1–100 for the matte the slag distribution coefficient between copper matte and iron silicate slag. Kaur et al. obtained a value of approximately 0.2 for the distribution coefficient of lead between copper metal and iron silicate slags, while it was around 2.5 for calcium ferrite slags at pO₂ 10^{−6} atm.¹⁰ The distribution coefficients determined in this work ($L_{Pb}^{m/s} = 0.4\text{--}2.1$) show that lead distributes quite

evenly between the matte and slag in FSF (DON) conditions. This is also supported by Sukhomlinov et al.⁹ who determined a matte–slag distribution coefficient of around 1 between a nickel–copper matte and iron silicate slag. In the EF, lead departs strongly in the matte, as calculated for both the matte–slag pairs.

Of all the trace elements studied, zinc shows by far the lowest recovery in the matte in both FSF and EF. The matte-to-slag distribution coefficient was as low as 0.03 in FSF, rising to 0.7 ± 0.03 in EF. The results are in line with the equilibrium distribution coefficients, between 0.016 and 0.6, determined by Sineva et al. for a copper (matte) smelting system with iron silicate slags.²⁶

The recovery of selenium in the FSF matte was highly effective, with the matte–slag distribution coefficients well over 500 for both the matte–slag pairs. These figures are in line with the results by Sukhomlinov et al.,⁹ who obtained distribution coefficients of 100–800 between a nickel–copper matte and iron silicate slag. The concentration of selenium in FSF slags in this study was close to the detection limit of LA-ICP-MS, and a value below 1 ppmw could be confirmed. The matte–slag distribution coefficient of Se was significantly lower in EF, with values of 57 and > 76 obtained for the two matte–slag pairs. It can be expected that the recovery of selenium to the matte may be stronger in more oxidizing systems, such as the FSF. This can also explain the difference in the distribution coefficient values between EF 1 and EF 2. The matte–slag distribution coefficients obtained are, however, slightly lower than what is expected from the equilibrium data by Sukhomlinov et al.⁹ The concentration of selenium in EF slag was roughly 2–3 times higher than in the FSF slag. This figure is high, considering that the feed of the EF is the FSF slag. However, considering that the total selenium present in the FSF slag including the entrained droplets is likely much higher than the chemically dissolved fraction, they are not excessive. Some fraction of FSF matte is also entrained to the EF during slag tapping. The same phenomena also affect the other trace elements that strongly depart in the FSF matte in the present conditions.

In the FSF, antimony departed preferentially in the matte, with the distribution coefficients in the range of 1–10. The results are of the same range as the equilibrium data between nickel matte and iron silicate slag of Font et al.,⁷ who obtained distribution coefficients of 1.4–100. The $L_{Sb}^{m/s}$ according to Font and Reddy¹⁴ varied between 5 and 100 and showed a strong increasing trend with increasing pO_2 . The distribution coefficients obtained here for the EF, > 3500 and > 5800 , were several orders of magnitude higher than in FSF. This is in accordance with the equilibrium metal–slag distribution coefficients in copper slag cleaning at iron saturation, determined by Hellstén et al.¹⁹ and Pagador

et al.,¹⁵ who obtained values in the range of 1000–10,000. However, the matte–slag distribution coefficient of antimony showed a much stronger negative correlation with oxygen partial pressure than the distribution coefficient of arsenic. The deportment of antimony can thus be controlled more strongly by adjusting pO_2 , i.e., the matte grade, than that of any other element studied.

The cobalt concentrations could be accurately determined using both LA-ICP-MS and EPMA, and they could thus be accurately determined even in the minor phases within the samples. In the FSF, cobalt distributed quite evenly between the matte and the slag, with a distribution coefficient of 1.0–1.3. The values agree with the equilibrium data by Piskunen et al.,⁴ Sukhomlinov et al.,⁹ and Font et al.⁷ between high-grade nickel and nickel–copper mattes, and iron silicate slags. Piskunen et al.⁴ obtained a matte–slag distribution coefficient of ~ 0.8 , Sukhomlinov et al.⁹ ended up with a value between 0.8 and 2.4, and Font et al.⁷ reported a value of ≈ 1 . Choi and Cho¹³ determined the cobalt distribution coefficient between matte and silica-saturated iron silicate slag in argon and CO–CO₂ mixtures over a wide range of nickel–copper matte grades. The distribution coefficients determined by them were slightly higher than those by the other research groups, ranging from 1.7 to 8.

Although the loss of cobalt to the FSF slag is substantial, its recovery in the EF matte is very effective. The matte–slag distribution coefficients obtained were as high as 24 and 47 for the EF matte–slag pairs. The measured distribution coefficient values were from batches with different reduction degrees, as shown by the magnetite concentrations. Cobalt behaves similarly to lead and antimony, distributing evenly between the matte and slag in the FSF, and more strongly towards the matte in the EF. The data obtained is in good agreement with the equilibrium observations by Grimsey,¹⁸ Pagador et al.,¹⁵ and Henao et al.,¹⁶ considering that the laboratory-scale measurements were mostly carried out at MgO-saturation, which favors the distribution in the matte.

CONCLUSION

The extensive sampling campaign at an industrial nickel smelter producing high-grade (DON) nickel matte with iron concentrations of 5–7 wt.% has shown with confidence that the matte-to-slag distribution coefficients of the main and minor metals closely follow the equilibrium observations obtained in laboratory conditions. Due to the complex mineralogy and small phase domains/grains generated in the sampling and cooling in industrial conditions, not all the minor and trace element concentrations could be measured with sufficient accuracy and resolution in the smallest phases using the EPMA and LA-ICP-MS techniques.

The present observations indicate the matte-to-slag distributions of the studied minority elements, As, Co, Sb, Se, Pb, Cu, and Zn in the high-grade matte smelting (FSF) and slag cleaning (EF) stages of direct nickel matte smelting. As a new quantification method for heterogeneous phases, the quantified EPMA element maps appear to be a useful tool for examining the detailed mineralogy of smelting slags.

This study complements the scattered element distribution data in the nickel slag cleaning conditions, and confirms the role of EF slag cleaning in the internal circulations of the conventional nickel matte smelting technologies, compared to the DON process where no circulation of EF matte exists. In such processes, the easily reducing oxides, such as arsenic, antimony, and lead, accumulate between converting and EF, whereas, in the DON process, they are deported in the EF matte stream and to the nickel refinery.

SUPPLEMENTARY INFORMATION

The online version contains supplementary material available at <https://doi.org/10.1007/s11837-024-06739-4>.

ACKNOWLEDGEMENTS

The use of RAMI Infrastructure funded by Academy of Finland and hosted jointly by Aalto University, Finnish Geological Survey and VTT is kindly acknowledged. One of the authors (OA) is indebted to Boliden Harjavalta for a research grant.

FUNDING

Open Access funding provided by Aalto University.

CONFLICT OF INTEREST

The authors declare that they have no conflict of interest.

OPEN ACCESS

This article is licensed under a Creative Commons Attribution 4.0 International License, which permits use, sharing, adaptation, distribution and reproduction in any medium or format, as long as you give appropriate credit to the original author(s) and the source, provide a link to the Creative Commons licence, and indicate if changes were made. The images or other third party material in this article are included in the article's Creative Commons licence, unless indicated otherwise in a credit line to the material. If material is not included in the article's Creative Commons licence and your intended use is not permitted by statutory regulation or exceeds the permitted use, you will

need to obtain permission directly from the copyright holder. To view a copy of this licence, visit <http://creativecommons.org/licenses/by/4.0/>.

REFERENCES

1. T. Mäkinen and P. Taskinen, *Miner. Process. Extract Metall.* 117(2), 86 <https://doi.org/10.1179/174328508X290867> (2008).
2. P. Taskinen, K. Seppälä, J. Laulumaa, and J. Poijärvi, *Trans. Inst. Min. Metall. Sect. C* 110(2), 101 <https://doi.org/10.1179/mpm.2001.110.2.101> (2001).
3. H. Johto, P. Latostenmaa, E. Peuraniemi, and K. Osara, *Extraction 2018*, in *The Minerals, Metals & Materials Series*. ed. by B. Davis, et al. (Springer, Berlin, 2018), p. 81. https://doi.org/10.1007/978-3-319-95022-8_6.
4. P. Piskunen, K. Avarmaa, H. O'Brien, L. Klemettinen, H. Johto, and P. Taskinen, *Metall. Mater. Trans. B* 49, 98 <https://doi.org/10.1007/s11663-017-1115-5> (2018).
5. M. Page, *Metall. Trans. B* 13(2), 141–152 (1982).
6. P. Taskinen, K. Avarmaa, H. Johto, and P. Latostenmaa, *Extraction 2018*, in *The Minerals, Metals & Materials Series*. ed. by B. Davis, et al. (Springer, Berlin, 2018). https://doi.org/10.1007/978-3-319-95022-8_25.
7. J. Font, M. Hino, and K. Itagaki, *Mater. Trans. JIM* 39(8), 834 <https://doi.org/10.2320/matertrans1989.39.834> (1998).
8. T. Hidayat, D. Shishin, D. Grimsey, P. Hayes, and E. Jak, *Metall. Mater. Trans. B* 49, 132 <https://doi.org/10.1007/s11663-017-1127-1> (2018).
9. D. Sukhomlinov, L. Klemettinen, O. Virtanen, Y. Lahaye, P. Latostenmaa, A. Jokilaakso, and P. Taskinen, *Can. Metall. Q.* 59(1), 67 <https://doi.org/10.1080/00084433.2019.1710386> (2020).
10. R. Kaur, D. Swinbourne, and C. Nexhip, *Miner. Process. Extract Metall.* 118(2), 65 <https://doi.org/10.1179/174328509X383890> (2009).
11. K. Monzen, S. Otsuka-Yao-Matsuo, and T. Omata, *J. MMIJ* 131, 65 <https://doi.org/10.2473/journalofmmij.131.65> (2015).
12. M. Kudo, E. Jak, P. Hayes, K. Yamaguchi, and Y. Takeda, *Metall. Mater. Trans. B* 31(1), 15 <https://doi.org/10.1007/s11663-000-0126-8> (2000).
13. N. Choi and W. Cho, *Metall. Mater. Trans. B* 28, 429 <https://doi.org/10.1007/s11663-997-0109-0> (1997).
14. J. Font and R. Reddy, *Miner. Process. Extract Metall.* 114(3), 160 <https://doi.org/10.1179/037195505X63349> (2005).
15. R. Pagador, M. Hino, and K. Itagaki, *Mater. Trans. JIM* 40(3), 255 (1999).
16. H. Henao, M. Hino, and K. Itagaki, *Mater. Trans.* 42(9), 1959 (2001).
17. K. Avarmaa, P. Taskinen, L. Klemettinen, H. O'Brien, and D. Lindberg, *J. Mater. Res. Technol.* 15(1), 719 (2021).
18. E. Grimsey, *Paul E. Queneau International Symposium: Fundamental Aspects vol. 1: Extractive Metallurgy of Copper, Nickel and Cobalt* (The Minerals, Metals and Materials Society, Warrendale, 1993), p. 1239.
19. N. Hellstén, L. Klemettinen, D. Sukhomlinov, H. O'Brien, P. Taskinen, A. Jokilaakso, and J. Salminen, *J. Sust. Metall.* 5, 463 <https://doi.org/10.1007/s40831-019-00237-7> (2019).
20. J. Pouchou and F. Pichoir, *Electron Probe Quantitation*, ed. K. Heinrich and D. Newbury, pp. 31–75 (Springer, Boston, 1991). https://doi.org/10.1007/978-1-4899-2617-3_4.
21. J. Donovan and T. Tingle, *Microscop. Microanal.* 2(1), 1 (1996).
22. T. May and R. Wiedmeyer, *Atom. Spectrosc.* 19(5), 150 (1998).
23. E. van Achterbergh, C. Ryan, S. Jackson, and W. Griffin, Appendix in: *Laser-ablation-ICPMS in the Earth Sciences—Principles and applications*, ed. P. Sylvester (Mineralogical Association of Canada, St. John, 2001), pp. 239–243.
24. J. Chen, A. Fallah-Mehrjardi, A. Specht, and H. O'Neill, *JOM* 74(1), 185 <https://doi.org/10.1007/s11837-021-04920-7> (2022).

25. M. Shuva, M. Rhamdhani, G. Brooks, S. Masood, and M. Reuter, *J. Clean. Prod.* 131, 795 <https://doi.org/10.1016/j.jclepro.2016.04.061> (2016).
26. S. Sineva, D. Shishin, M. Shevchenko, P. Hayes, and E. Jak, *J. Mater. Res. Technol.* 23, 5280 <https://doi.org/10.1016/j.jmrt.2023.02.120> (2023).

Publisher's Note Springer Nature remains neutral with regard to jurisdictional claims in published maps and institutional affiliations.